Structural origins for the high plasticity of a Zr–Cu–Ni–Al bulk metallic glass

D.D. Qu [a], K.-D. Liss [b], Y.J. Sun [c], M. Reid [d], J.D. Almer [e], K. Yan [b,d], Y.B. Wang [f], X.Z. Liao [f], J. Shen [a,*]

[a] *School of Materials Science and Engineering, Harbin Institute of Technology, Harbin 150001, China*
[b] *Australian Nuclear Science and Technology Organisation, Lucas Heights, NSW 2234, Australia*
[c] *Department of Physics, School of Science, Tianjin Polytechnic University, Tianjin 300387, China*
[d] *Faculty of Engineering, University of Wollongong, Wollongong, NSW 2522, Australia*
[e] *Advanced Photon Source, Argonne National Laboratory, Argonne, IL 60439, USA*
[f] *School of Aerospace, Mechanical and Mechatronic Engineering, The University of Sydney, Sydney, NSW 2006, Australia*

Abstract

The structural origins for the high plasticity of a $Zr_{53}Cu_{18.7}Ni_{12}Al_{16.3}$ (at.%) bulk metallic glass are explored. Under plastic flow conditions, in situ synchrotron high-energy X-ray diffraction reveals that the atomic strain saturates to the closest packing in the longitudinal direction of the applied load while atoms yield in the transverse plane. Scanning electron microscopy investigation reveals that global plasticity benefits from abundant shear band multiplication and interactions. Atomic level flows are seen to accompany profuse shear bands. The plasticity enhancement of this metallic glass benefits from such atomic level flows. Atomic level flow facilitates the activation of shear transformation zones that further self-assemble to promote shear band multiplication. On the other hand, it also mitigates the shear band propagation that prevents catastrophic shear band extension.
© 2012 Acta Materialia Inc. Published by Elsevier Ltd. All rights reserved.

Keywords: Bulk metallic glass; Plasticity; In situ high-energy X-ray diffraction; Structural anisotropy

1. Introduction

The room-temperature plasticity of bulk metallic glasses (BMGs) is achieved primarily through the accumulation of abundant localized shear bands. To enhance the plasticity of a BMG, it is essential to promote shear band multiplication and to prevent the dominant shear band from extending catastrophically throughout the whole BMG [1]. Numerous metallic glass composites have been developed to compensate for the limited plasticity of the amorphous matrix with the addition of tough crystalline reinforcements [2]. Plastic deformation treatments using techniques like high-pressure torsion [3] and cold rolling [4] have been used to improve the plasticity of BMGs to some extent. Unfortunately, only a limited number of monolithic BMGs have been found to possess high plasticity [5–8]. It has been demonstrated that the structural origins responsible for such high plasticity are strongly correlated to a high Poisson's ratio [5], structural heterogeneity at the atomic scale [6] or nanoscale [7], and high free volume fraction [8]. Additionally, the plasticity is always correlated to the elastic properties; for example, a low ratio of shear modulus to bulk modulus (G/B) corresponds to good plasticity [5,9–11]. However, solid evidence from the atomic level structures in favor of profuse shear band multiplication and interactions is inadequate. Microscopically, it has been proposed that the plastic deformation of metallic glasses starts from the activation of shear transformation zones (STZs), which initially involve a few atoms and then grow

---

* Corresponding author. Tel.: +86 451 86403196.
E-mail address: junshen@hit.edu.cn (J. Shen).

by self-assembling [12]. Nonetheless, the structural entities responsible for this shear transformation have only been realized through computer simulations; experimental evidence is lacking [13–15].

Synchrotron high-energy X-ray diffraction techniques [16] have been increasingly used to explore the atomic level mechanisms responsible for the structural changes caused by heating [17,18] and loading [19–23]. Unlike the periodically arranged structure of a crystalline material, atoms in a metallic glass array without any long-range order, implying that the structure of a metallic glass should be inherently isotropic. Under a uniaxial load, however, the structure of the material becomes anisotropic [23–26]. Even deformation at the atomic level is not fully affine [26,27]. A metallic glass is furthermore shown to contain a quarter of liquid-like clusters without any resistance to an external load [23]. Therefore, even when the metallic glass experiences elastic deformation macroscopically, at the atomic level it is accompanied with anelastic deformation [23] which has been proposed to be realized through bond reorientation [24,26]. Previous in situ structural characterizations have mainly focused on the elastic deformation stage [20,21] and homogeneous flows [24,26]; structural changes during the shear banding dominated deformation are rarely reported.

In this paper, the structural origins of the high plasticity of a $Zr_{53}Cu_{18.7}Ni_{12}Al_{16.3}$ (Zr53) BMG [28] are studied upon quasi-static compression using in situ synchrotron high-energy X-ray diffraction. In the plastic stage, the apparent strain at atomic level saturates in the longitudinal direction (the loading direction), while it rises continuously in the transverse plane (perpendicular to the loading direction). Abundant atomic level flows are seen to accompany profuse shear banding, which further contributes to the plasticity enhancement of the Zr53 BMG.

2. Experimental

A cylindrical Zr53 BMG with a diameter of 2 mm was used in this experiment. Four elements – Zr (99.9%), Cu (99.99%), Ni (99.9%) and Al (99.99%), with a nominal composition of $Zr_{53}Cu_{18.7}Ni_{12}Al_{16.3}$ (at.%) – were mixed and arc melted in a Ti-gettered pure argon atmosphere four times, then drop cast into a copper mold. Structural characterizations using X-ray diffraction on a D/MAX-RB apparatus and high-resolution transmission electron microscopy performed in a JEOL 3000F microscope confirmed the amorphous nature of the material. The specimen for electron microscopy was prepared by mechanical grinding followed by twin-jet electropolishing. Samples with a length to diameter aspect ratio of 2:1 were used for ex situ quasi-static compression testing, which was conducted using an Instron 4500 machine at a strain rate of $4 \times 10^{-4} \, s^{-1}$. The morphology of the fracture surfaces was analyzed using Hitachi S-470 and S-570 scanning electron microscopes.

In situ synchrotron high-energy X-ray diffraction with a characteristic X-ray energy of 90 keV was carried out at the 1-ID-C beamline of the Advanced Photon Source (APS), Argonne National Laboratory, combined with a stand-alone hydraulic load frame on a MTS-858 set-up with a maximal force of $\pm 15 \, kN$ [29]. The energy resolution ($\Delta E/E$) of the characteristic energy of the monochromatic X-ray was 1.5×10^{-3}. A fine beam of $100 \times 100 \, \mu m^2$ was transmitted through the Ø 2 mm sample during the compression process. Diffraction patterns were recorded by a MAR-165 CCD detector (2048 × 2048 pixels, 80 × 80 μm^2 pixel size) at a recording speed of 8 s per frame. The two-dimensional (2-D) diffraction patterns were cleared from digital outlayers by a four-pixel median filter using the ImageJ program. Then the structure factor $S(Q)$ in the reciprocal space was obtained by azimuthally integrating the 2-D diffraction pattern using the software package dataRring [30]. Q is the scattering vector that lies close to the plane perpendicular to the incident beam. The isotropic and anisotropic parts of the structure factor $S(Q)$ were fully analyzed in dataRring, and later verified by the Fit2-D and PDFgetX2 software. The 2-D circular diffraction patterns were divided into 72 sectors, with 5° per sector. The isotropic and anisotropic parts of the atomic density function $\rho(r)$ were obtained via the Bessel transformation as proposed by Suzuki et al. [24].

3. Results

3.1. Mechanical properties

Fig. 1a shows the compressive engineering stress–strain curve of the Zr53 BMG. The material yields at a strength of $\sigma_y = 1880$ MPa and reaches its maximum compressive strength at $\sigma_m = 2160$ MPa. Further increase in the plastic strain is accompanied by stress reduction until fracture. The total plastic strain ε_p is 14.5%. These findings indicate that $Zr_{53}Cu_{18.7}Ni_{12}Al_{16.3}$ is a new BMG that possesses high plasticity.

The stress–strain curve associated with the plastic deformation is characterized by flow serrations, as depicted in Fig. 1b. This phenomenon is caused by abundant shear band multiplication and interactions during compressive loading [31]. The morphology of the fracture surface is shown in Fig. 1c–e. From Fig. 1c, the compressive shear fracture angle is measured to be 44.8°. As pointed out by Zhang et al. [32], taking the plasticity into account, this value can be corrected to 40.7°, which is a typical value of the initial shear angle of the primary shear band in such material [32]. Areas marked with arrows in an enlarged image shown in Fig. 1d presented solid evidence of strong shear band interactions. The vein-like pattern on the fractured surface shown in Fig. 1e, which results from abundant localized shear flows [33], confirms the strong shear band interactions. Therefore, the high plasticity observed in the Zr53 BMG is due in large part to the profuse shear band multiplication and interactions; this finding is also supported by our recent transmission electron microscopy investigation results [34].
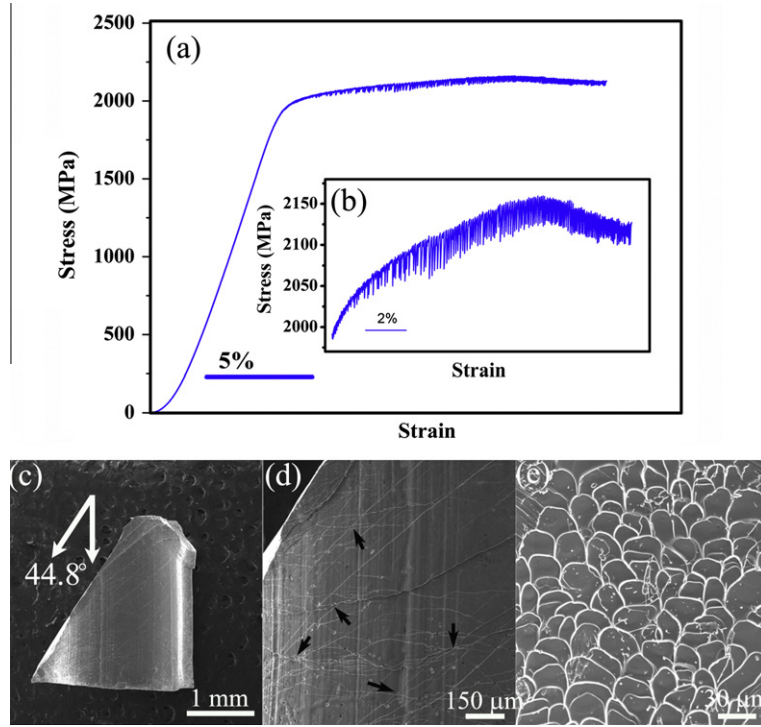
Fig. 1. (a) A compressive stress–strain curve of the Zr53 BMG at room temperature. (b) Enlargement of the shear serration in the plastic stage. (c) A side-view scanning electron micrograph of a fractured sample. (d) An enlarged side-view image near the fracture plane. (e) A vein pattern on the fracture surface.

3.2. In situ diffraction during compression

It is well known that the isotropic atomic packing structure of metallic glasses becomes anisotropic under uniaxial loading, resulting in an elliptical 2-D diffraction ring, as observed by Wang et al. [35]. Poulsen et al. [19] first observed the atomic level apparent strain that was later evaluated by others [20–22] using the equation

$$\varepsilon(\sigma, \psi) = \frac{q_1(0, \psi)}{q_1(\sigma, \psi)} - 1 \qquad (1)$$

where q_1 is the position of the first peak maximum on the 2-D diffraction circle, σ is the corresponding compressive stress and ψ is the azimuthal angle around the 2-D diffraction center, starting from the loading direction. The apparent strain $\varepsilon(\sigma, \psi)$ can be expressed by [19–22]

$$\varepsilon(\sigma, \psi) = \varepsilon_{11}(\sigma) \cdot \cos^2 \psi + \gamma(\sigma) \cdot \sin \psi \cdot \cos \psi + \varepsilon_{22}(\sigma)$$
$$\cdot \sin^2 \psi \qquad (2)$$

Eq. (2) contains three strain tensor components – the longitudinal compressive strain $\varepsilon_{11}(\sigma)$, the shear strain in the plane perpendicular to the incident beam direction $\gamma(\sigma)$ and the transverse expansive strain $\varepsilon_{22}(\sigma)$. For consistency, strain evaluation via Eq. (1) was undertaken for both the positions q_1 and q_2, of the first and second diffraction maxima, respectively. To determine the values of q_1 and q_2 precisely, both the first and second maximum peaks are mathematically fitted [36]. Then the off-center correction is performed by averaging the two opposite peak

positions on the diffraction pattern, leading to a measure of half of the diameter of the pattern [29]. The fitting error bars plotted in all of the figures below are at the same scale as the symbol size.

Fig. 2 shows the strain dependence on the azimuthal angle determined through q_1 and q_2. As shown in Fig. 2a and b, the fitted apparent strains (solid lines) evaluated for q_1 and q_2 agree very well with the results calculated using Eq. (2), except that the data scattering of q_2 is more significant than that of q_1. Fig. 2c and d presents the overall atomic strain variations with respect to the loading step during the compressive test from the elastic to plastic stages calculated based on q_1 and q_2, respectively. It is demonstrated that, except for some noise present during the early steps of the test, the evaluated apparent strains are indeed periodically distributed with respect to the azimuthal angle.

Fig. 3 shows the fitted longitudinal compressive strain $\varepsilon_{11}(\sigma)$, the in-plane shear strain $\gamma(\sigma)$ and the transverse expansive strain $\varepsilon_{22}(\sigma)$ evolution against the loading steps. It can be seen that the two sets of strain tensors corresponding to positions q_1 and q_2 agree well with each other. The amplitude of the longitudinal compressive strain $\varepsilon_{11}(\sigma)$ increases rapidly and saturates at -1.7%, while the maximum transverse expansive strain $\varepsilon_{22}(\sigma)$ grows gradually up to 0.8%. It is noticeable that the apparent transverse strain $\varepsilon_{22}(\sigma)$ increases further in the plastic stage, even after the longitudinal compressive strain $\varepsilon_{11}(\sigma)$ has reached saturation. The in-plane shear strain $\gamma(\sigma)$ remains zero in the elastic stage but deviates slightly from the zero strain
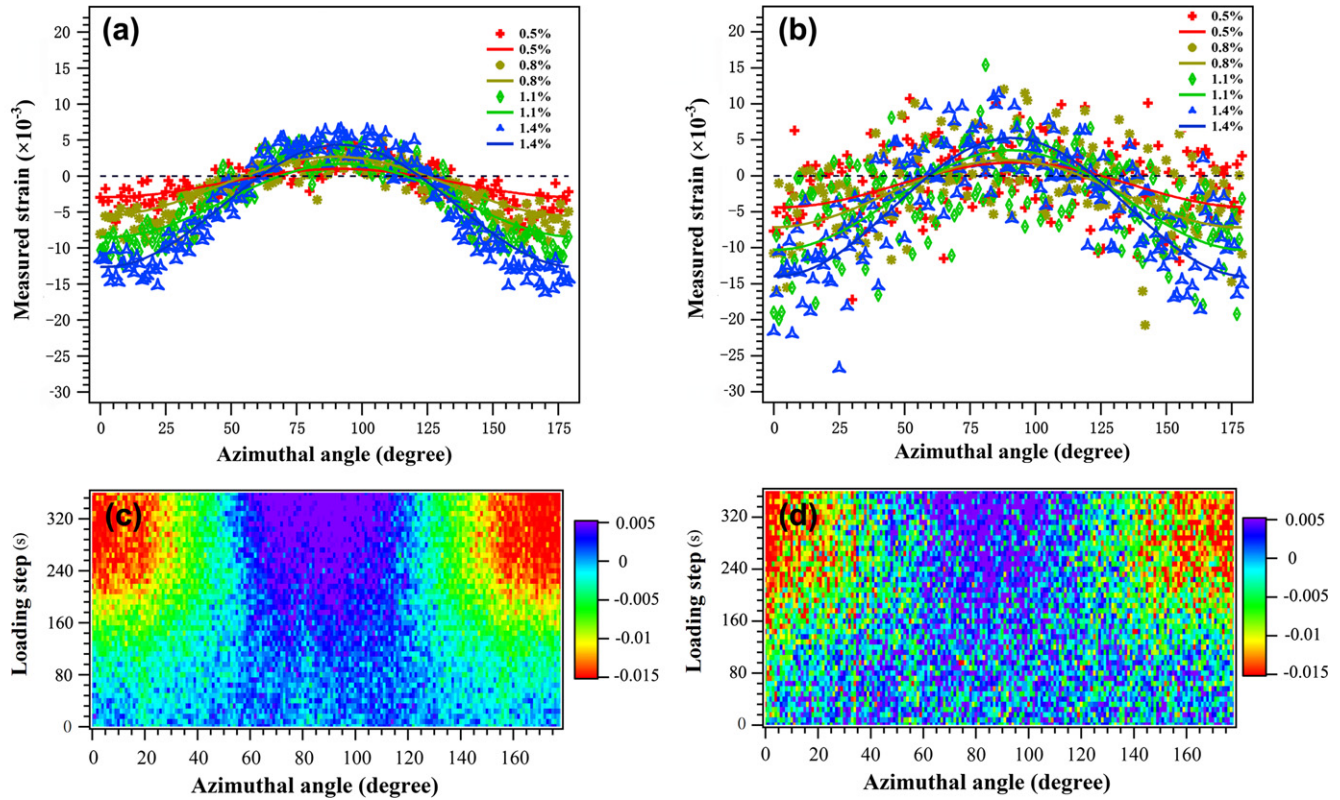
Fig. 2. Azimuthal angle dependence of the apparent strain measured via the first and the second maximum diffraction peak positions q_1 (a) and q_2 (b) on structure factor $S(Q)$ for four typical elastic strains in compression (the scattered symbols) according to Eq. (1), together with the fitted lines based on Eq. (2). The compilation of the azimuthal angle-dependent apparent strains obtained through Eq. (1) are represented in (c) (via q_1) and (d) (via q_2) from elastic to plastic deformation.
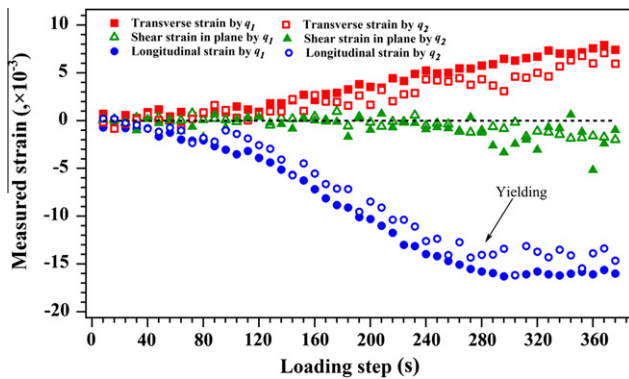

Fig. 3. The variation in the apparent longitudinal strain ε_{11}, transverse strain ε_{22} and in-plane shear strain γ obtained through fitting q_1 and q_2 during compression. The arrow indicates the yielding point, while the dashed line presents the baseline for zero in-plane shear strain.
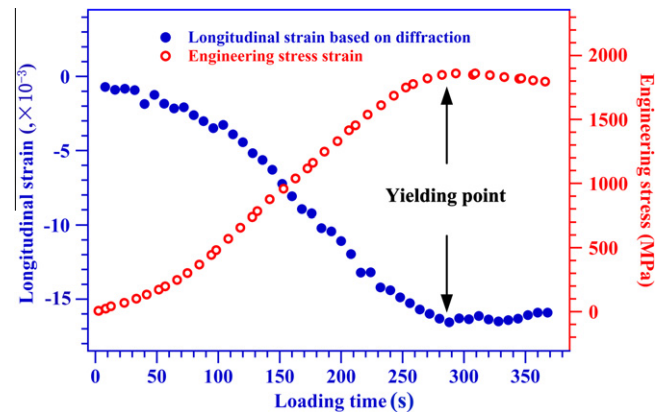

Fig. 4. The evolution of the apparent atomic level longitudinal strain obtained through q_1 and the engineering stress with respect to the loading time.

baseline in the plastic stage, implying that a shear deformation mode proceeds therein. The average value of Poisson's ratio in the elastic stage is calculated to be 0.36. This is in excellent agreement with the value of 0.352 measured by a complementary ultrasonic technique.

In Fig. 4, the variations of the apparent longitudinal compressive strain $\varepsilon_{11}(\sigma)$ and the engineering stress with respect to the loading time are compared. It is clearly seen that the material yields in coincidence with the saturation

of $\varepsilon_{11}(\sigma)$. This agreement implies that the deformation mechanism of Zr53 BMG is indeed caused by atomic rearrangements, as opposed to the motion of dislocation that is the primary cause of plastic deformation in crystalline materials [12,37]. The apparent engineering plastic strain, calculated through the saturated longitudinal strain, is 4% (see Fig. 4). This value agrees well with the macroscopic strain of 4.15% measured on the engineering stress–strain curve, despite the elastic strains not being comparable

because of the influence caused by the low degree of stiffness of the loading frame. The compressive elastic limit is 1.7%, which is close to the elastic limit of 2% typically observed in BMGs [38]. The plasticity of 4% signifies that the deformation is still far from fracture, where the total plasticity can be as high as 14.5%; however, shear bands and shear serrations have been generated.

Regarding the anisotropy during uniaxial loading, as manipulated in the literatures [20,22–24,26], the directional structure factor $S(Q)$ and the atomic density function $\rho(r)$ can be expanded into spherical harmonics, i.e.

$$S(\boldsymbol{Q}) = \sum_{l,m} S_l^m(Q) \cdot Y_l^m(\boldsymbol{Q}/Q) \quad (3)$$

and

$$\rho(\boldsymbol{r}) = \sum_{l,m} \rho_l^m(r) \cdot Y_l^m(\boldsymbol{r}/r) \quad (4)$$

The corresponding components $S_l^m(Q)$ and $\rho_l^m(r)$ in Eqs. (3) and (4) are correlated through the spherical Bessel transformation,

$$\rho_l^m(r) = \frac{i^l}{2\pi} \int S_l^m(Q) \cdot J_l(Q \cdot r) \cdot Q^2 dQ \quad (5)$$

where $J_l(Q \cdot r)$ is the lth-order Bessel function with the variable $Q \cdot r$. Assuming the uniaxial deformation is isotropic in the plane perpendicular to the loading direction, the parameter m in Eqs. (3)–(5) could be reduced to zero. That higher order components $l > 2$ can be ignored and symmetric considerations allow only even values of l reduces the series to the $l = 0$ and $l = 2$ components only, with $S_0^0(Q)$, $\rho_0^0(r)$ and $S_2^0(Q)$, $\rho_2^0(r)$, for the isotropic and anisotropic parts of the directional structure function and the atomic density function, respectively. These functions describe the deformation ellipse that is well known in residual strain measurements and is often applied to evaluations by diffraction on polycrystalline materials [29]. Consequently, the structure factor $S(Q)$ and the atomic density function $\rho(r)$ in any direction ψ ($0 \leqslant \psi \leqslant 360°$) in the plane perpendicular to the incident beam are given, respectively, by

$$S(Q, \psi) = S_0^0(Q) \cdot \sqrt{\frac{1}{4\pi}} + S_2^0(Q) \cdot \sqrt{\frac{5}{16\pi}} \cdot (3\cos^2\psi - 1) \quad (6)$$

and

$$\rho(r, \psi) = \rho_0^0(r) \cdot \sqrt{\frac{1}{4\pi}} + \rho_2^0(r) \cdot \sqrt{\frac{5}{16\pi}} \cdot (3\cos^2\psi - 1) \quad (7)$$

Inversely, substituting two directional structure factors into the left side of Eq. (6), $S_0^0(Q)$ and $S_2^0(Q)$ can be readily obtained. The two directions are usually adjusted parallel and perpendicular to the loading direction, setting ψ to be 0° and 90°, respectively [20,24,29]. Subsequently, the directional atomic density function $\rho(r, \psi)$ for the anisotropic structure can be obtained using Eqs. (5) and (7).

The evolution of the isotropic and the anisotropic part of the structure factor, $S_0^0(Q)$ and $S_2^0(Q)$, respectively, is shown in Fig. 5 for both the elastic and plastic stages. Only

four apparent strain levels in the elastic stage ($\varepsilon_e = 0.5\%$, 0.8%, 1.1% and 1.4%) and five strain levels in the plastic stage ($\varepsilon_p = 0.8\%$, 1.6%, 2.4%, 3.2% and 4.0%) are presented for clarity. As can be seen in Fig. 5a and b, the isotropic part of the structure factor $S_0^0(Q)$ undergoes relatively small changes during the deformation process and is characterized by a maximum peak followed by several decaying oscillations, typical for metallic glasses. The anisotropic part $S_2^0(Q)$ reflects the difference between the longitudinal and transverse directions. As shown in Fig. 5c, when $S_0^0(Q)$ undergoes its first maximum peak, $S_2^0(Q)$ first drops to form a negative valley then increases to form a positive peak, finally decreasing again and oscillating around zero. As indicated by the arrow in Fig. 5c, $S_2^0(Q)$ increases proportionally to the elastic strain during elastic deformation, whereas it is almost independent of plastic strain in the plastic stage (Fig. 5d).

The detailed variations in the positive and negative amplitudes of $S_2^0(Q)$ are plotted in Fig. 6. As can be seen, both the positive and negative amplitudes of $S_2^0(Q)$ increase gradually, though at different rates, in the elastic stage. In the plastic stage, the negative amplitude continues to grow, while the positive amplitude approaches saturation. This indicates that in the elastic stage the anisotropic behavior of the atomic structure is primarily dominated by one mechanism, which is the affine change in the interatomic distance; however, in the plastic stage the mechanism is more complex, and is likely related to the directional atomic level flows.

According to the transformation of Eq. (5), the isotropic and anisotropic parts of the atomic density function $\rho(r)$ are obtained through $S_0^0(Q)$ and $S_2^0(Q)$, as shown in Fig. 7. Similar to the variation trend of the structure factor, the isotropic part of the atomic density function $\rho_0^0(r)$ shows very small changes at both the elastic (Fig. 7a) and plastic (Fig. 7b) stages. $\rho_0^0(r)$ is mainly characterized by a primary nearest neighbor correlation peak, followed by decaying oscillations (see also Ref. [17]). The noise in the anisotropic part $\rho_2^0(r)$ in Fig. 7c and d is relatively large due to the limited Q-range of the data acquisition. However, the trend of the amplitude of $\rho_2^0(r)$ in the range corresponding to the nearest neighbor on $\rho_0^0(r)$ can still be observed approximately. It varies proportionally with the elastic strain, as indicated in Fig. 7c. The change in the amplitude in the plastic stage is much less obvious, as can be seen in Fig. 7d.

In summary, the anisotropic behavior of the Zr53 BMG is reflected clearly by the evolution of $S_2^0(Q)$ and $\rho_2^0(r)$. Both of the two anisotropic functions exhibit saturation in the plastic stage, which is related to the directional structural changes in real space, as mentioned above. Therefore, using Eq. (7), we calculated the longitudinal and transverse atomic density functions, $\rho_L(r)$ and $\rho_T(r)$, and these are shown in Fig. 8 for the complete deformation process. Very slight changes in the nearest neighbor peak can be seen from Fig. 8a to d. The nearest neighbor peak is fitted by a Gaussian function to determine the peak position r_1
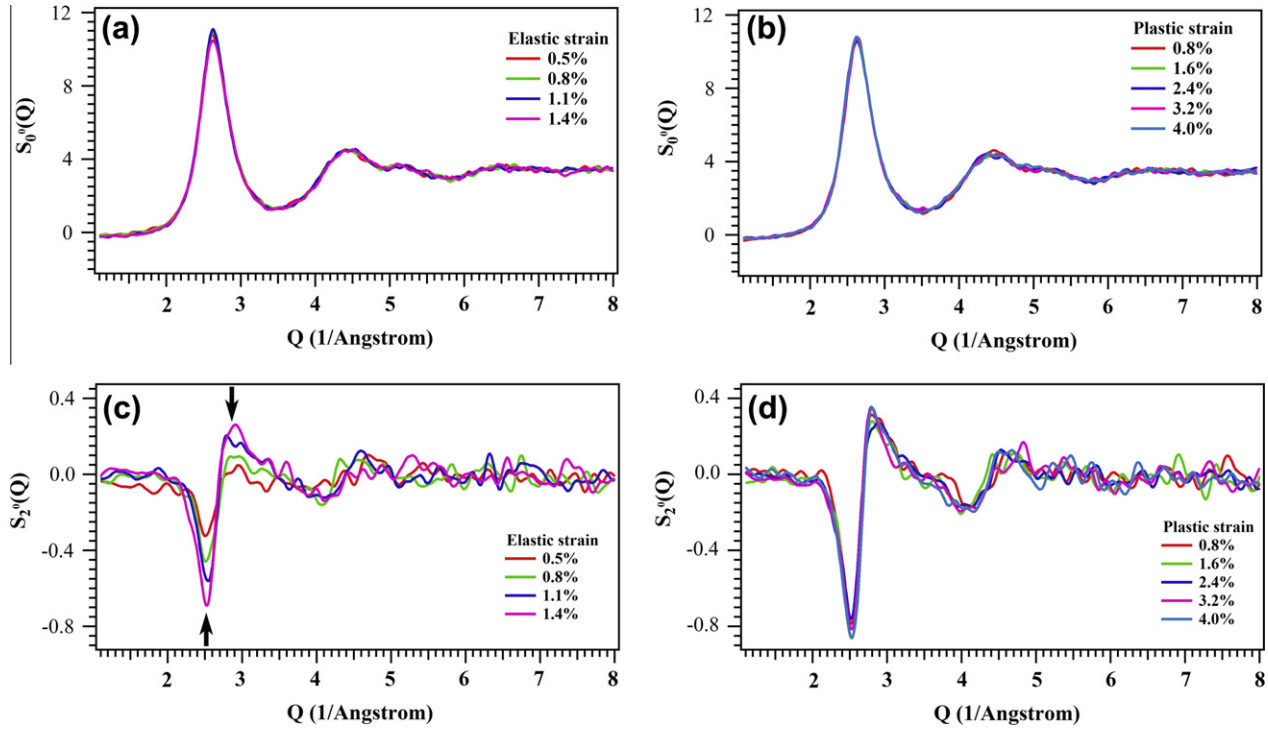
Fig. 5. Evolution of the isotropic part of the structure factor $S_0^0(Q)$ in the elastic (a) and plastic (b) stages and the anisotropic part $S_2^0(Q)$ in the elastic (c) and plastic (d) stages. For clarity, only four elastic and five plastic strain levels are shown. The corresponding strains are described in the legends of (a and b). The arrows in (c) shows the positions where the amplitude of $S_2^0(Q)$ grows as the external strain increases.
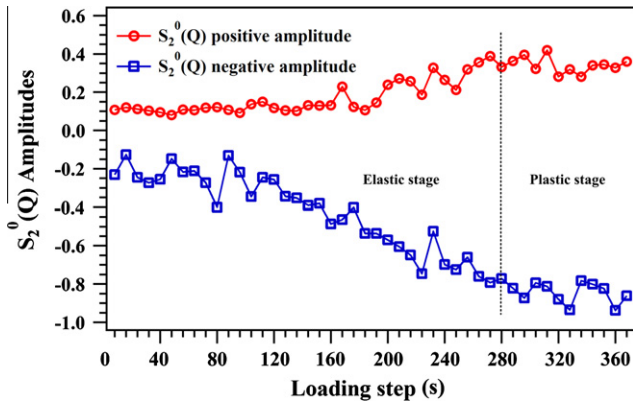

Fig. 6. Variations of the positive and negative amplitudes for the anisotropic part of the structure factor $S_2^0(Q)$.

and the peak width w, which describe the mean interatomic distance and the deviation from the mean interatomic distance, respectively.

Fig. 9 shows the variation in the nearest neighbor peak position r_1 and the peak width w of the longitudinal and transverse atomic density functions vs. loading. As shown by the evolution trend of r_1, the mean interatomic distance diminishes in the loading direction at a much faster rate than its transverse expansion. It is obvious that the longitudinal interatomic distance remains static during the plastic stage, while the transverse expansion continuously increases. The peak width w exhibits a similar trend as r_1, diminishing in the loading direction but expanding laterally. However,

the rate of change of w is much lower than that of r_1. A similar trend was also reported by Hufnagel et al. [25]. As suggested, the sharpening of the atomic density function peak is correlated with an elevated average atomic-level hydrostatic stress $\langle p \rangle$ [25,39] and indirectly implies the atomic rearrangement occurring in some large dilatation regions, which in turn increases the local hydrostatic stress. Moreover, opposite tendencies of the slight change in w in the longitudinal and transverse directions (shown in Fig. 9b) indicate that such atomic rearrangement has different mechanisms. The large dilatation regions gradually diminish in the longitudinal direction but grow in the transverse plane, which is consistent with what is observed via the strain anisotropy shown in Fig. 3.

4. Discussion

4.1. Diffraction based strain evaluation

The strain evaluation method based on Eq. (1) is valid for cases where strain at the atomic level is affine or all atoms move by the same factor during deformation [20,23]. Hence, this method is not applicable in situations where the strain is non-affine or the deformation is anisotropic, such as in polycrystalline materials. However, from the viewpoint of diffraction, the scattering result reveals the real spatial changes in the scale of the wavelength of the probing beam, such as the variation in interatomic distances. Therefore, instead of interpreting the ratio given
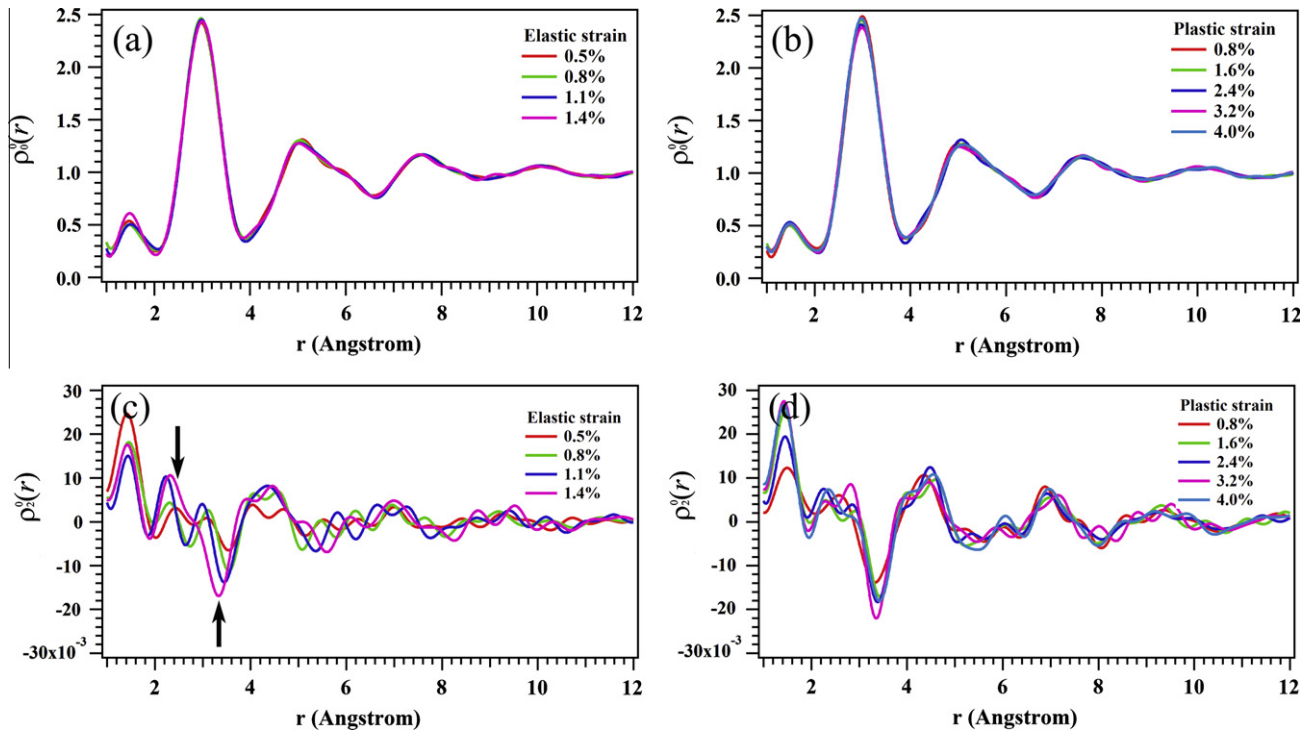
Fig. 7. Evolution of the isotropic part of the atomic density function $\rho_0^0(r)$ in the elastic (a) and plastic (b) stages and the anisotropic part of the atomic density $\rho_2^0(r)$ in the elastic (c) and plastic (d) stages. Curves shown in this figure have the same strain levels as in Fig. 5. The arrows in (c) show the positions where the amplitude of $\rho_2^0(r)$ varies as the elastic strain increases.
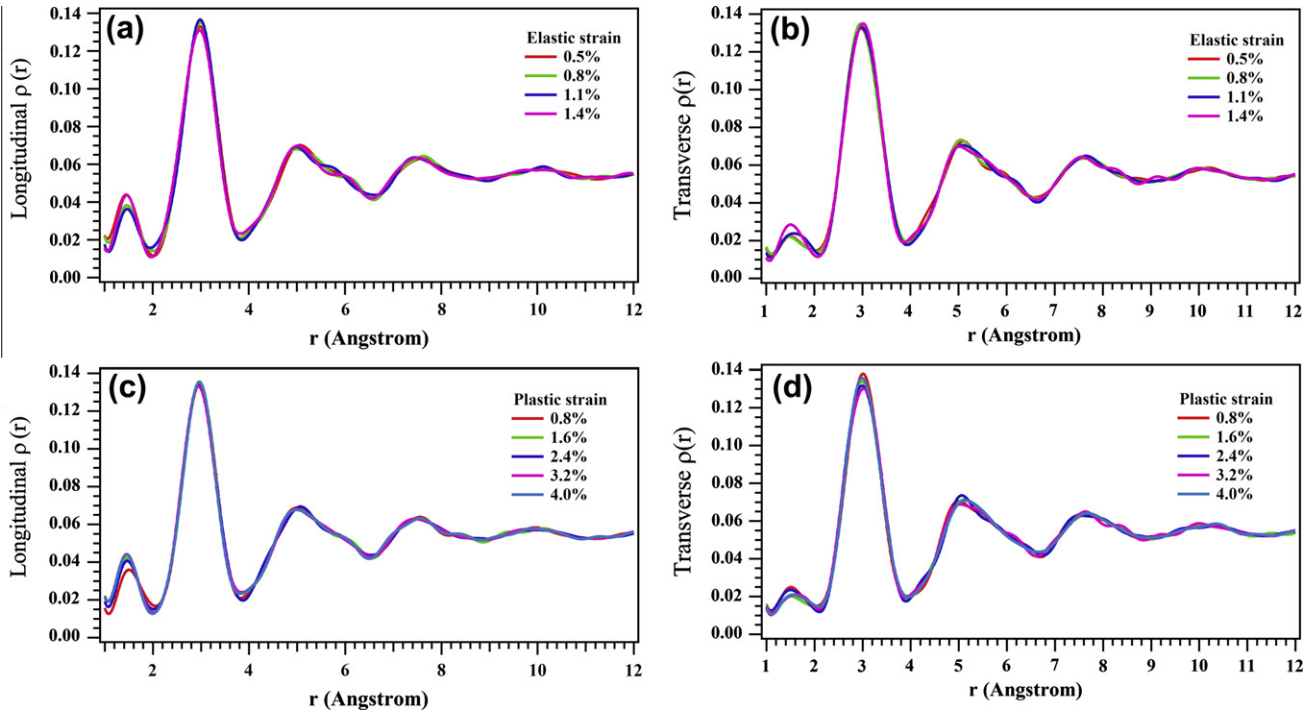

Fig. 8. Evolution of the longitudinal (a and c) and transverse (b and d) atomic density functions $\rho_L(r)$ and $\rho_T(r)$ in the elastic and plastic stages. All the curves are shown at the same strain levels as in Fig. 5.

in Eq. (1) through the deformation strain, it would be more reasonable to explain this variation by relating it to the real space changes in different azimuthal angle directions. Nonetheless, it should be kept in mind that the real space changes reflected by the reciprocal space peak positions (e.g. q_1 and q_2) as used in Eq. (1) can be induced by
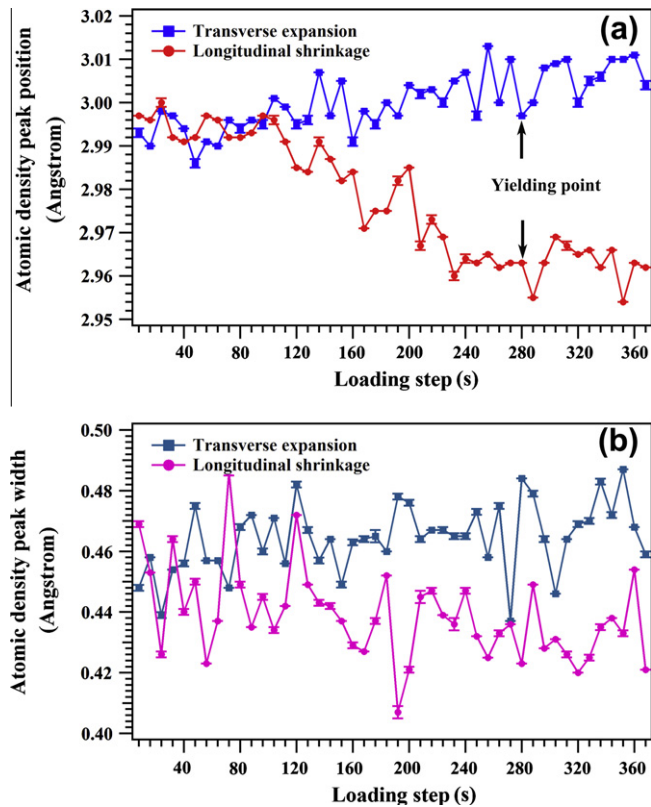
Fig. 9. Variation of the nearest neighbor peak position r_1 (a) and the peak width w (b) of the longitudinal and transverse atomic density functions $\rho_L(r)$ and $\rho_T(r)$ vs. the loading step. The fitting errors noted are on the same scale as the symbol size. To clearly show the trend of the peak width w variation, the curve for the transverse expansion in (b) is raised by 0.02 Å in the vertical direction.

different mechanisms, such as elastic strain, anelastic strain, creep strain and deformation-induced dilatation [40]. Elaborated mechanisms of the deformation require the apparent strain to be reduced into different components. For instance, it is reported that during elastic deformation the affine elastic strain can be obtained through the proportional coefficient by fitting the derivative of the isotropic atomic density function $r \cdot \frac{d\rho_0^0(r)}{dr}$ to the anisotropic part $\rho_2^0(r)$ [23,24]. However, the decomposition of the above-mentioned strain components and even further manipulation are hampered by the limited resolution of the data herein, which require further high-resolution investigation.

As discussed by Cargill [41], Suzuki et al. [24] and Ma et al. [42], the first peak of the structure factor $S(Q)$ primarily describes the medium-range order correlation in real space well beyond the first peak of $\rho(r)$, while higher order peaks contribute to the short-range order of the first nearest neighbors. Therefore, it is necessary to compare the apparent strains based on both the short- and medium-range orders that are evaluated from the peak positions of the atomic density function and the structure factor, as shown in Fig. 10. It is interesting to note that, in spite of the noise in the short-range order, all the three kinds

of apparent strains obtained through q_1, q_2 and r_1 coincide with each other in both the longitudinal and transverse directions. This implies that the apparent interatomic distances in both the short- and medium-range orders change at the same apparent rate. In particular, the phenomenon that apparent strains in both the short- and medium-range orders evolve in the same manner reflects that the atomic level response to the external stress is homogeneous.

4.2. Structural origin for the high plasticity

The plastic deformation of the Zr53 BMG is primarily fulfilled by profuse shear band multiplication and interactions, as demonstrated in Fig. 1. Previous investigations indicate that the dimensions of shear bands are extremely small, with typical widths of 10–20 nm and a volume fraction of $\sim 10^{-6}$ [43,44]. Compared with the illuminated volume given by a $100 \times 100\ \mu m^2$ X-ray beam and a 2 mm transmitted sample thickness, the contribution to the diffraction intensity from shear bands can thus be reasonably ignored. As a result, the mechanism for the plastic deformation revealed by the diffraction technique relies virtually solely on the atomic level flows behind the shear band interactions.

The longitudinal strain becomes saturated in the plastic regime, beyond the yielding point, as underlined by both the apparent strains from the short- and medium-range orders displayed in Fig. 10. Furthermore, in a displacement-controlled experiment, although the apparent atomic level strain remains static, the sample still undergoes macroscopic deformation, producing the engineering strain shown in Fig. 4. At the same time, atomic strain continues to increase laterally. This implies that atoms yield as hard spheres during uniaxial compression: when maximal compressed along the longitudinal direction, they yield laterally.

Assuming that the constituent atoms of the BMG behave analogously to ideal hard-sphere balls in the plastic stage, prohibiting any additional compressive strain, the
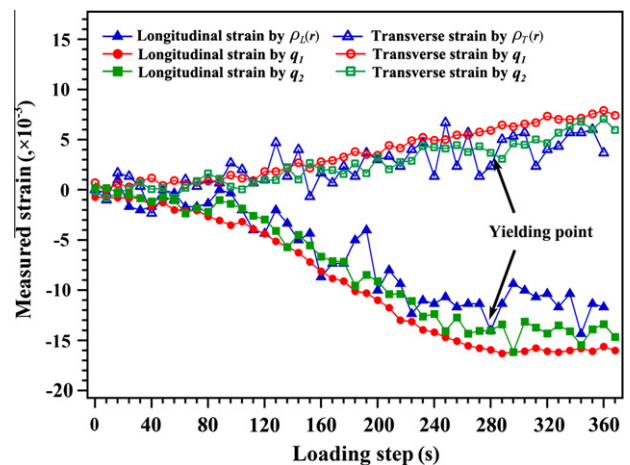

Fig. 10. Comparison of the longitudinal and transverse strains obtained through q_1 and q_2 of the structure factor $S(Q)$, and the nearest neighbor peak position r_1 of the atomic density functions $\rho_L(r)$ and $\rho_T(r)$.

macroscopic plastic strain could then only be achieved by pushing some balls away from the loading direction and forcing them to flow laterally in the plane perpendicular to the loading direction, which is similar to the interpretation of bond reorientation [24]. The continuous increase in the transverse strain further indicates that the lateral expansion in the plastic deformation comprises the pure lateral out-pushing atomic flow mechanism and flow dilatation, which correlate with the frustration of the icosahedral short-range order [45]. Therefore, in addition to the shear band interactions, abundant homogeneous flow at the atomic level contributes significantly to the plastic strain.

The plasticity enhancement of metallic glass at room temperature is primarily dominated by shear band accumulation. Shear band formation has been described as an activation of stress-assisted STZs and an assisted autocatalytic assembly on the maximum shear plane to trigger strain localization [46,47]. In addition, strain localization in a shear band is also influenced by a strain rate mismatch between the shear band and the glassy matrix, and it is the stress concentrator at the shear front that drives the shear band propagation [1]. Recently, Liu et al. [48] proposed that good ductility of metallic glass correlates with a low shear band initiation energy, a weak shear band propagation driving force and a strict shear band extension limit. The high atomic flowability demonstrated above favors the activation of STZs and thus structurally lowers the shear band initiation energy. This also allows the glassy matrix to effectively relax the external stress and to reduce the stress mismatch between the shear band and the glassy matrix. The relaxed stress mismatch in turn weakens the driving force for shear band propagation. Thus, the plastic deformation process can be interpreted as follows: due to spatial or temporal perturbation in the homogeneous atomic level flow, the first few shear bands are generated and propagate quickly. The propagating and interacting shear bands in turn enhance the atomic flow and the shear band multiplication. In this way, the deformed metallic glass increasingly accommodates the local strains, which eventually accumulate to form a large macroscopic strain. Simultaneously, the relaxed glass matrix mitigates the strain rate mismatch between the shear band and the matrix, which consequently reduces the driving force for the shear band propagation and prevents long-distance propagation throughout the material. Therefore, the plasticity enhancement observed in the Zr53 BMG is attributed to both the abundant homogeneous atomic level flow and the profuse shear band multiplication and interactions.

5. Conclusion

In conclusion, the $Zr_{53}Cu_{18.7}Ni_{12}Al_{16.3}$ alloy is a new BMG with high plasticity. Upon yielding and plastic deformation, the atomic level apparent strain saturates along the loading direction but continuously expands in the lateral plane. Homogeneous atomic level flow coexists with large-scale shear banding. Such atomic level flow facilitates the activation of STZs, which further promotes shear band multiplication. On the other hand, this atomic level flow relaxes the stress in the glassy matrix, which thus mitigates the shear band propagation driving force and prevents catastrophic shear band extension. Both the atomic level homogeneous flow and the profuse shear band multiplication and interactions account for the plasticity enhancement of this material. However, due to the limited resolution of the diffraction data, elaborate anisotropic strain evaluations are hampered. As a result, higher resolution in situ diffraction analysis is still required to study in more detail the accurate deformation mechanisms in both the macroscopic elastic and inhomogeneous plastic stages.

References

[1] Schuh CA, Hufnagel TC, Ramamurty U. Acta Mater 2007;55:4067.
[2] Eckert J, Das J, Pauly S, Duhamel C. J Mater Res 2007;22:285.
[3] Wang YB, Qu DD, Wang XH, Cao Y, Liao XZ, Kawasaki M, et al. Acta Mater 2012;60:253.
[4] Lee MH, Lee KS, Das J, Thomas J, Kuhn U, Eckert J. Scripta Mater 2010;62:678.
[5] Schroers J, Johnson WL. Phys Rev Lett 2004;93:255506.
[6] Das J, Tang MB, Kim KB, Theissmann R, Baier F, Wang WH, et al. Phys Rev Lett 2005;94:205501.
[7] Liu Y, Wang G, Wang R, Zhao D, Pan M, Wang W. Science 2007;315:1385.
[8] Chen LY, Fu ZD, Zhang GQ, Hao XP, Jiang QK, Wang XD, et al. Phys Rev Lett 2008;100:075501.
[9] Lewandowski JJ, Wang WH, Greer AL. Philos Mag Lett 2005;85:77.
[10] Poon SJ, Zhu AW, Shiflet GJ. Appl Phys Lett 2008;92:261902.
[11] Cheng YQ, Cao AJ, Ma E. Acta Mater 2009;57:3253.
[12] Argon AS. Acta Metall 1979;27:47.
[13] Falk ML, Langer JS. Phys Rev E 1998;57:7192.
[14] Mayr SG. Phys Rev Lett 2006;97:195501.
[15] Delogu F. Phys Rev Lett 2008;100:255901.
[16] Liss KD, Bartels A, Schreyer A, Clemens H. Texture Microstruct 2003;35:219.
[17] Qu D, Liss K-D, Yan K, Reid M, Almer JD, Wang Y, et al. Adv Eng Mater 2011;13:861.
[18] Wang XL, Almer J, Liu CT, Wang YD, Zhao JK, Stoica AD, et al. Phys Rev Lett 2003;91:265501.
[19] Poulsen HF, Wert JA, Neuefeind J, Honkimaki V, Daymond M. Nat Mater 2005;4:33.
[20] Mattern N, Bednarcik J, Pauly S, Wang G, Das J, Eckert J. Acta Mater 2009;57:4133.
[21] Das J, Bostrom M, Mattern N, Kvick A, Yavari AR, Greer AL, et al. Phys Rev B 2007;76:092203.
[22] Wang G, Mattern N, Pauly S, Bednarcik J, Eckert J. Appl Phys Lett 2009:95.

[23] Dmowski W, Iwashita T, Chuang CP, Almer J, Egami T. Phys Rev Lett 2010;105:205502.
[24] Suzuki Y, Haimovich J, Egami T. Phys Rev B 1987;35:2162.
[25] Hufnagel TC, Ott RT, Almer J. Phys Rev B 2006;73:064204.
[26] Dmowski W, Egami T. J Mater Res 2007;22:412.
[27] Waire D, Ashby MF, Logan J, Weis J. Acta Metall 1971;19:779.
[28] Sun YJ, Qu DD, Huang YJ, Liss KD, Wei XS, Xing DW, et al. Acta Mater 2009;57:1290.
[29] Liss KD, Yan K. Mater Sci Eng A 2010;528:11.
[30] Liss K-D, Yeoh LA, Yan K. DataRring Software Package. ANSTO; 2004–2012.
[31] Hufnagel TC, El-Deiry P, Vinci RP. Scripta Mater 2000;43:1071.
[32] Zhang ZF, He G, Zhang H, Eckert J. Scripta Mater 2005;52:945.
[33] Bian Z, Chen GL, He G, Hui XD. Mater Sci Eng A 2001;316:135.
[34] Qu DD, Wang YB, Liao XZ, Shen J. Scripta Mater 2012;67:332.
[35] Wang G, Mattern N, Bednarčík J, Li R, Zhang B, Eckert J. Acta Mater 2012;60:3074.
[36] Bednarcik J, Chen LY, Wang XD, Jiang JZ, Franz H. Metall Mater Trans A 2012;43:1558.
[37] Johnson WL, Samwer K. Phys Rev Lett 2005;95:195501.
[38] Inoue A. Acta Mater 2000;48:279.
[39] Srolovitz D, Egami T, Vitek V. Phys Rev B 1981;24:6936.
[40] Mear FO, Vaughan G, Yavari AR, Greer AL. Philos Mag Lett 2008;88:757.
[41] Cargill GS. Solid State Phys 1975;30:227.
[42] Ma D, Stoica AD, Wang XL. Nat Mater 2009;8:30.
[43] Jiang WH, Atzmon M. Acta Mater 2003;51:4095.
[44] Spaepen F. Acta Metall 1977;25:407.
[45] Cao AJ, Cheng YQ, Ma E. Acta Mater 2009;57:5146.
[46] Homer ER, Schuh CA. Acta Mater 2009;57:2823.
[47] Demetriou MD, Johnson WL, Samwer K. Appl Phys Lett 2009;94:191905.
[48] Liu Z, Li R, Wang G, Wu S, Lu X, Zhang T. Acta Mater 2011;59:7416.